JOURNAL OF MARINE RESEARCH

The *Journal of Marine Research,* one of the oldest journals in American marine science, published important peer-reviewed original research on a broad array of topics in physical, biological, and chemical oceanography vital to the academic oceanographic community in the long and rich tradition of the Sears Foundation for Marine Research at Yale University.

An archive of all issues from 1937 to 2021 (Volume 1–79) are available through EliScholar, a digital platform for scholarly publishing provided by Yale University Library at https://elischolar.library.yale.edu/.

Requests for permission to clear rights for use of this content should be directed to the authors, their estates, or other representatives. The *Journal of Marine Research* has no contact information beyond the affiliations listed in the published articles. We ask that you provide attribution to the *Journal of Marine Research.*

Yale University provides access to these materials for educational and research purposes only. Copyright or other proprietary rights to content contained in this document may be held by individuals or entities other than, or in addition to, Yale University. You are solely responsible for determining the ownership of the copyright, and for obtaining permission for your intended use. Yale University makes no warranty that your distribution, reproduction, or other use of these materials will not infringe the rights of third parties.

Mixing rates across the Gulf Stream, Part 2: Implications for nonlocal parameterization of vertical fluxes in the surface boundary layers

by R. Inoue[1,2], R. R. Harcourt[1] and M. C. Gregg[1]

ABSTRACT

The turbulent kinetic energy (TKE) budget of the surface mixed layer is evaluated at wintertime stations occupied in the vicinity of the strong Gulf Stream (GS) jet. The nonlocal K-profile parameterization (KPP) of vertical fluxes is combined with observed hydrography and meteorology to diagnose TKE production. This KPP-based production is averaged over the surface mixed layer and compared with corresponding averages of observed TKE dissipation rate from microstructure measurements, under assumptions of a homogeneous steady-state balance for the layer-averaged TKE budget. The KPP-based TKE production estimates exceed the mean observed boundary layer dissipation rates at occupied stations by up to an order of magnitude. In cases with strong upper ocean shear, the boundary layer depths predicted by the bulk Richardson number criteria of KPP tend to be deeper than indicated by observed dissipation rates, and thereby including strong entrainment zone shear contributes excessively to the KPP-based diagnosis of TKE production. However, even after correcting this diagnosis of mixed layer depth, the layer-averaged production still exceeds observed dissipation rates. These results have several possible implications, including: (1) KPP tends to overestimate vertical momentum flux in cases with strong shear due to geostrophically balanced thermal wind, unbalanced submesoscale dynamics, or entrainment driven by mixed layer inertial oscillations; (2) a mean local TKE balance does not hold in baroclinic mixed layers due to radiation of inertial waves, divergence in horizontal TKE flux or an inverse cascade to larger scales; and (3) both the boundary layer depth and the remaining TKE budget discrepancies indicate the limited validity of mixed layer models in the simulation of submesoscale ocean phenomena.

1. Introduction

Eighteen Degree Water (EDW) is the North Atlantic subtropical mode water that is formed by air-sea heat exchange south of the Gulf Stream (GS) (Worthington, 1959). It has a large subsurface thermal capacity, suggesting that its formation and dissipation could impact climate (Marshall, 2005; CLIMODE Group, 2009). This motivated the study of EDW as part of the CLIVAR (Climate Variability and Predictability) program. A companion paper (Inoue *et al.,* 2010, hereafter PART 1) presents results from wintertime microstructure measurements across the GS during a CLIMODE (CLIVAR Mode Water

---

1. Applied Physics Laboratory, University of Washington, 1013 NE 40th Street, Seattle, Washington, 98105-6698, U.S.A.

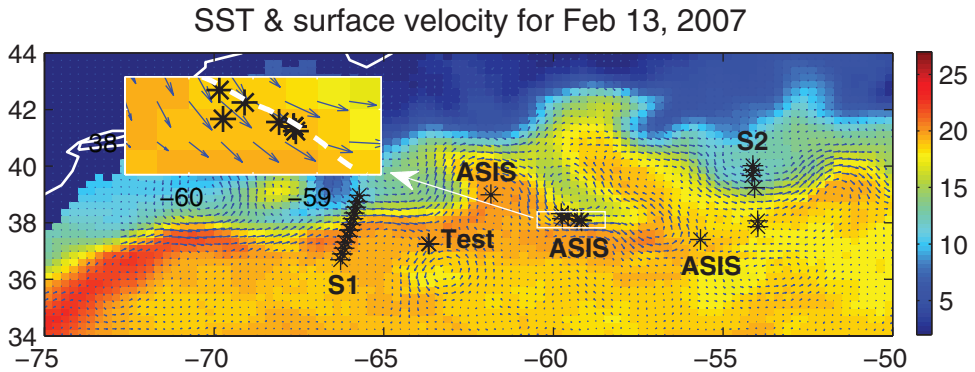2. Corresponding author: *email: rinoue@apl.washington.edu*

Figure 1. Sea-surface temperature (SST) and velocity calculated from surface slope at the beginning of the CLIMODE cruise measurements. Locations of all AMP profiles are superimposed. Though SST changed in the Gulf Stream, the position and intensity of the stream remained similar in subsequent satellite images.

Dynamics Experiment) cruise in February 2007 and suggests that mixed layer cooling south of the GS is the primary mechanism for EDW formation. Here we examine the validity and implications of boundary layer parameterizations within the observed mixed layers because they are important for verifying the predictability of EDW in ocean general circulation models (OGCMs).

In this study, we compare TKE production estimates based on K-profile parameterization (KPP; Large *et al.,* 1994) against *in-situ* dissipation measurements. This comparison assumes that the number and duration of measurements here are sufficient to test the underlying assumptions of a quasi-steady and homogeneous balance for TKE production and dissipation terms averaged over the surface mixed layer. The TKE production is estimated by applying KPP to shipboard atmospheric data, CTD casts, and 150-kHz ship ADCP data. Observed dissipation rates and CTD data were obtained using the Advanced Microstructure Profiler (AMP), covering depths from 16 m to around 1000 m. The AMP carries two airfoils to measure centimeter-scale velocity fluctuations, Neil Brown conductivity cells, and FP07 thermistors. The TKE dissipation rate ε is estimated by assuming that turbulence is isotropic at this scale (Shay and Gregg, 1986; Gregg, 1999). To compare with production estimates that are layer-averaged to remove TKE transport divergence terms, each dissipation profile is also averaged over the layer. Velocity data are averaged over the half-hour period of the AMP downcast with valid data limited to depths between 8 m and around 200 m. This means that production estimates are based on shear measurements averaged over durations comparable to the timescale mixed layer turbulence, while only one dissipation profile is obtained from a single downcast during that period. This does raise the possibility that observed levels can often lie below the mean if temporal variations in layer-mean dissipation are lognormally distributed. Station points are shown in Figure 1. Further details of these observations and data are provided in PART1.

The choice of KPP to diagnose turbulent vertical viscosities and diffusivities in the surface boundary layer is motivated by several considerations. KPP is a widely used mixing parameterization in OGCMs, in part because the required computational cost is lower than higher order closure schemes (e.g., Mellor and Yamada, 1982). Unlike KPP, the down-gradient flux assumptions of most such second moment closures entail buoyancy profiles within mixed layers that differ substantially from observations or turbulence-resolving numerical solutions (e.g., Fig. 13 in Burchard and Bolding, 2001). The application here of parameterized eddy diffusivities to observed hydrography in free convectively forced layers, therefore, also determines our selection of a model such as KPP that admits counter-gradient buoyancy fluxes. KPP has been tested against large eddy simulations and *in-situ* measurements (e.g., Large and Gent, 1999) and tuned to reproduce the simulated vertical fluxes and the *in-situ* evolution of bulk mixed layer properties. It is widely used in many kinds of OGCMs. However, we are unaware of any direct comparison against microstructure measurements. KPP uses empirical functions and constants that are in part determined from atmospheric boundary layer observations in steady-state homogeneous conditions (Large *et al.,* 1994). Submesoscale and subinertial timescale dynamics in the heterogeneous environments of fronts can potentially impact the validity of KPP at a point where the role of turbulent mixing is most vital to ocean models' predictive skill.

Some skepticism is expected over the comparisons argued here. Parameterizations of turbulent vertical mixing are generally "lesser evils" that are primarily expected to correspond to observed ocean mixing on the basis of equivalence in long-term averages of the rates of change in upper ocean geopotential energy, and through their repercussions on much larger scale ocean dynamics. Similar comparisons for second order turbulence closure models (Peters and Baumert, 2007) based on "nudging" simulations toward observed mean hydrography demonstrate large $O(10)$ factors between observed and model dissipation that are only reduced to $O(1)$ discrepancies with extensive averaging.

However, the presumption of applying a mixing parameterization to vertically smoothed station data averaged over only $O(1)$ hour in this study is roughly matched by its recent applications in numerical simulations with 100-m to 1-km horizontal model resolution (e.g., Boccaletti *et al.,* 2007; Capet *et al.,* 2008; Thomas, 2008). Since KPP is designed to match atmospheric boundary layer observations in steady-state homogeneous conditions, it is appropriate to question how or why the validity of vertical mixing schemes may be limited at this extreme standard of resolving submesoscale and subinertial timescale dynamics in baroclinic environments, and whether conclusions drawn from its use are consequently impacted. It is also expedient to address these questions in an empirical context, because modeling studies present difficult choices between domain scales, turbulence resolution, and complex oceanic realism. Because a high degree of statistical scatter is to be expected, meaningful conclusions must rise significantly above the noise.

In Section 2, methods for the diagnosis of vertical momentum and buoyancy fluxes using KPP combined with observations are explained, and boundary layer depths D_{Ri} are diagnosed from KPP's critical bulk Richardson number criterion. Bulk TKE production is

estimated by integrating the parameterized source term profiles over the mixed layer, and this prediction tends to be larger than the mean observed dissipation rate. In Section 3 this overprediction of TKE production is shown to be due partly to the diagnosis of layer depths D_{Ri} that exceed observed mixing depths D_ε based on dissipation profiles. Substituting for D_{Ri} an alternative layer depth D_K, inferred by comparing measured ε to the subsurface parameterizations of KPP, improves but does not fully resolve the TKE budget discrepancy. In Section 4 possible sources of this discrepancy are investigated. Comparisons are made between observed velocities and the nondimensional speed gradient profiles that underlie KPP predictions. We also discuss the impact of lateral density gradients on KPP, and attempt to modify the vertical velocity scale in KPP to include submesoscale processes in several cases. However, those modifications do not fully resolve the discrepancy. In Section 5 we instead accept the KPP velocity scale and examine the broader set of GS stations for the potential impacts of near-inertial wave radiation and submesoscale processes on the mixed layer TKE budget. Results are summarized and further implications are discussed in Section 6.

2. Diagnosis of vertical mixing and TKE production

This section details how KPP was used to estimate vertical fluxes of momentum, heat and salinity, and to diagnose the layer-averaged TKE production. It then argues the basis under which production and dissipation rates may be compared, and presents an initial comparison that is subsequently revised in Section 3.

a. Diagnosis of KPP eddy viscosity and diffusivities

Vertical fluxes $\overline{w'\xi'}$ in KPP have the general form

$$\overline{w'\xi'} = -K_\xi^{KPP}\left(\frac{\partial \bar{\xi}}{\partial z} - \gamma_\xi\right), \tag{1}$$

for fluctuating ξ' and ensemble or horizontally averaged mean $\bar{\xi}$ variables indicating scalars of temperature θ, salinity S, density ρ or buoyancy b, or indicating momentum vectors $\mathbf{U} = [U, V]$. The same vertical eddy diffusivity K_ρ^{KPP} applies to all scalars; K_ν^{KPP} is the eddy viscosity for momentum flux, and γ_ξ is a nonlocal gradient accounting for vertical flux transport divergence. In the standard version used here (Large *et al.*, 1994), the nonlocal transport term γ_ξ is only nonzero within the mixed layer and only for active scalar variables under convective conditions, where γ_b produces a counter-gradient buoyancy flux $\overline{w'b'} > 0$ at certain stably stratified depths $\partial \bar{b}/\partial z > 0$ in the middle to lower layer. This feature was instrumental in our decision to use KPP to analyze wintertime GS observations where surface buoyancy loss was prevalent. Within a mixed layer, KPP components K_ρ^{KPP}, K_ν^{KPP}, and γ_b are nonlocal functions of surface fluxes and of the surface boundary layer depth D. Below the layer a local parameterization determines

subsurface values of K_ρ^{KPP} and K_ν^{KPP} as functions of the local gradient Richardson number.

The depth D in KPP is defined by the shallowest level where the bulk Richardson number,

$$Ri_{bulk} = -\frac{(b_r - b)z}{|\mathbf{U}_r - \mathbf{U}|^2 + U_t^2}, \tag{2}$$

exceeds a critical value of 0.3. The reference buoyancy b_r and velocity $\mathbf{U}_r$ are averages over the top of 10% of the layer. In free convection the depth D should be near the largest entrainment buoyancy flux, at about -0.2 times the surface value. The turbulent velocity scale U_t depends on the strength of boundary layer turbulence, but due to large $|\mathbf{U}_r - \mathbf{U}|$ levels it does not have a significant role here. We denote this layer depth as D_{Ri} to distinguish it from other empirical layer depths defined in Section 3a.

Within the boundary layer, KPP predicts

$$K_\xi^{KPP}(\sigma) = DG(\sigma)w_\xi(\sigma), \tag{3}$$

as a function of $\sigma = -z/D$, a nondimensional shape function $G(\sigma)$ (O'Brien, 1970), and turbulent velocity scale profile $w_\xi(\sigma)$. The nonlocal transport term γ_b depends upon surface buoyancy flux J_b^0, D, and $w_b(\sigma)$. The profile of $w_\xi(\sigma)$ is a function of the convective $w* = (J_b^0 D)^{1/3}$ and frictional $u* = \sqrt{\tau_0/\rho_{surf}}$ velocity scales for surface stress τ_0, where ρ_{surf} is water density at the sea surface. For unstable conditions $w_\xi(\sigma)$ also depends upon empirical nondimensional shear profiles $\phi_\xi(\zeta)$ developed for atmospheric boundary layers (e.g., Vickers and Mahrt, 1999) via $w_\xi(\sigma) = \kappa u*/\phi_\xi(\zeta)$. Here, κ is the von Karman constant and $\zeta = -z/L_{MO}$ scales depth on the Monin-Obukhov length $L_{MO} = -u*^3/\kappa J_b^0$. The above outline of KPP is meant primarily to point out the dependencies in KPP on layer depth D and the distinction of the nonlocal and local prescriptions for eddy fluxes applied above and below D, respectively. For more complete details see Large *et al.* (1994).

b. Vertical fluxes and TKE production

To calculate KPP boundary layer depths and fluxes, observed profiles are first heavily smoothed, because KPP is designed for numerical models where prognostic variables represent profiles of much broader grid- or larger ensemble-averaged properties. The AMP CTD data are smoothed with an 8-m box-car filter and interpolated to the 4-m ADCP grid. To remove mixed layer turbulent motion, a half-hour average is used for ADCP data, and noisy profiles due to changes in ship course or speed are excluded. Above the 8-m top ADCP depth, filtered CTD and ADCP data are extrapolated linearly to the surface, and these points are used only to calculate the boundary layer depth D. Several different smoothing schemes were tested, but our basic results are not sensitive to small variations in this method. This analysis was applied to 21 out of 30 stations occupied. Nine profiles were excluded because either ADCP coverage did not encompass all of the contiguous regions
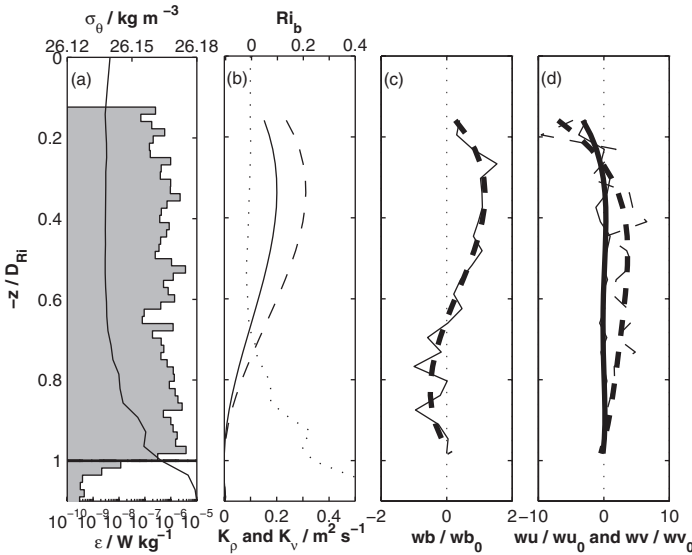
Figure 2. Vertical profiles in AMP21198. Vertical axis is depth normalized by $D_{Ri} = 112$ m. (a) Observed potential density averaged over 8 m, observed ε averaged over every 2 m, with horizontal line D_{Ri}. (b) predicted vertical eddy diffusivity (dashed) and viscosity (solid), (c) and (d) buoyancy flux within the boundary layer from KPP normalized by surface buoyancy flux and momentum fluxes for x- (solid line) and y-direction (dotted line) from KPP normalized by surface momentum flux. Thick lines show smoothed fluxes.

of high boundary-layer dissipation levels below the surface, the AMP conductivity probe showed apparent drifts, or meteorological buoyancy flux suggested that re-stratification was under way.

Momentum and buoyancy fluxes are obtained by combining the KPP-based estimates of D_{Ri}, K_{ρ}^{KPP}, K_{ν}^{KPP}, and γ_b with the vertical gradients of the smoothed profiles of observed buoyancy frequency squared N^2 and shear $d\mathbf{U}/dz$. Figure 2 shows an example of a KPP-based diagnostic calculation of D_{Ri} and vertical fluxes at station AMP21198. Depth is normalized by $D_{Ri} = 112$ m. In this profile, negative buoyancy flux due to local stratification is dominant just above D_{Ri} and the normalized buoyancy flux further up changes sign. The curved buoyancy flux profile within the well-mixed layer may be a statistical variation, it may imply that γ_b is too large at mid-depths, or there may be compensating divergences in horizontal buoyancy flux and the combined effect changes mixed layer temperature more uniformly.

c. TKE production and observed dissipation

In an advected mixed layer reference frame, the budget for changes in TKE $k = u_i' u_i'/2$ is averaged over observed depths 16 m $< -z \leq D_{Ri}$, where $i = (x, y, z)$. This bulk TKE budget

$$\langle Dk/Dt \rangle = \langle \Psi \rangle + \langle \partial\Phi_i/\partial x_i \rangle - \langle \varepsilon \rangle, \tag{4}$$

balances net shear and buoyant production $\langle \Psi \rangle$, divergence $\langle \partial\Phi_i/\partial x_i \rangle$ in TKE transport $\Phi_i = u_i'k + \rho_0^{-1}u_i'p'$ by advection or waves, dissipation $\langle \varepsilon \rangle$ and the growth or "tendency" $\langle Dk/Dt \rangle$. In this section we assume, as is conventional in boundary layer parameterizations, that contributions from horizontal fluxes are negligible. The KPP-based estimate of TKE production $\langle \Psi_{KPP} \rangle = \langle Sh \rangle + \langle J_b \rangle$ therefore contains only contributions from vertical shear $Sh = K_v^{KPP}|d\mathbf{U}/dz|^2$ and buoyancy flux $J_b = -K_\rho^{KPP}(N^2 - \gamma_b)$. Neglecting as well horizontal TKE fluxes $\langle \partial\Phi_x/\partial x + \partial\Phi_y/\partial y \rangle \cong 0$, transport divergence contributes only at the upper and lower observed mixed layer boundaries, $\langle \partial\Phi_i/\partial x_i \rangle \cong (D - 16m)^{-1}\bar{\Phi}_z\big|_{-D}^{-16m}$. We use fourth order polynomial fitting to further smooth momentum and buoyancy flux profiles (Fig. 2) in estimating the contributions to $\langle \Psi_{KPP} \rangle$ TKE production from vertical shear and buoyancy flux. Other smoothing methods were considered, including a linear fit to velocity and several different low pass filters, but these did not significantly change the overall pattern of results reported here.

With typical frictional velocity forcing scales of 1–3 cm s^{-1} and O(100) m layer depths, tendency contributions to the TKE budget are also assumed to be small $\langle Dk/Dt \rangle \cong 0$, because (1) the corresponding $O(1)$ hour turbulence time scales for structures of size $\sim D$ are similar to the duration of observations at each station, and TKE levels are therefore near steady state, and (2) the $> O(1)$ day synoptic time scales governing surface forcing entail slow TKE changes on corresponding time scales, less than $O(10^{-9}) - O(10^{-8})$ m^2 s^{-3}, smaller than $\langle \varepsilon \rangle$. Our implicit assumption of equivalence between measurements in the ship's and mean mixed layer's reference frames is expected to contribute only random errors.

Losses of TKE through flux $\bar{\Phi}_z\big|_{-D}$ to depths below D from the mixing layer by turbulent and internal wave transport are traditionally assumed small in the bulk TKE budget (Niiler and Kraus, 1977). Losses to downward propagating gravity waves in recent turbulence-resolving simulations of wind and wave-driven layers (Polton *et al.,* 2008) were found to deplete shallow ($\sim$20 m) mixed layer TKE budgets on a $\sim$6-day time scale. Downward fluxes at near-inertial frequencies drain energy with decay time scales between $O(1)$ and many inertial periods (D'Asaro *et al.,* 1995; Alford, 2001). Although this energy is thought to come out of the inertially oscillating bulk mixed layer momentum, i.e., $\langle U_i \rangle^2/2$, there may be internal wave losses $(16m - D)^{-1}\bar{\Phi}_z\big|_{-D}$ from the TKE budget at the lower boundary. While the presence of strong horizontal gradients in potential vorticity near the GS may increase decay rates significantly, our working assumption is to neglect the loss, revisiting this possibility in Section 5.

In general, TKE production under these conditions of atmospheric wind stress and buoyancy loss is expected to be surface intensified, and down-gradient TKE flux assumptions imply that any transport into the averaging depths from above 16 m would be positive $(16m - D)^{-1}\bar{\Phi}_z\big|_{-16m} > 0$. Similarly, including Stokes TKE production terms (e.g., McWilliams *et al.,* 1997; Kantha and Clayson, 2003) in this region of downfront prevailing wind and
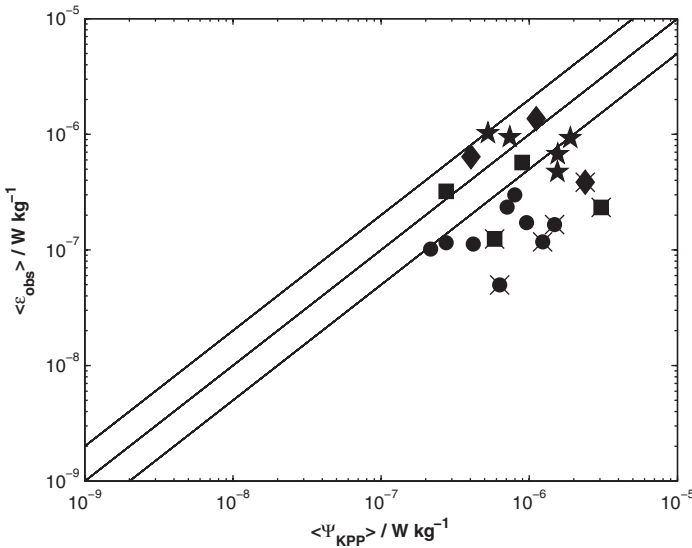
Figure 3. Bulk comparison between observed ε and predicted ε from KPP (5). Solid lines show factors of 0.5, 1 and 2. Crosses indicate profiles where $\langle Sh \rangle / \langle \varepsilon_{obs} \rangle > 4$. Filled circles are south of the GS. Filled squares are near and in the GS. Filled diamonds are north of the GS. Filled stars are profiles near the ASIS buoy. These plots contain one dot per profile.

waves would contribute positively to $\langle \Psi_{KPP} \rangle$, as would any lateral shear production by frontolytic down-gradient fluxes of horizontal momentum, omitted from $\langle Sh \rangle$ above.

Given the above assumptions, we expect the KPP-parameterized TKE production to be a lower bound for the bulk observed dissipation averaged over the same depths:

$$\langle \Psi_{KPP} \rangle = \langle Sh \rangle + \langle J_b \rangle \leq \langle \varepsilon_{obs} \rangle, \tag{5}$$

Many assumptions made to yield (5) are not expected to hold for any single profile, but only in the mean. Some statistical scatter in this comparison is reduced here by averaging vertically over the mixed layer. Coherent trends in our lower bound estimate of the TKE budget discrepancy $\langle \Psi_{KPP} \rangle - \langle \varepsilon_{obs} \rangle > 0$ may therefore serve to indicate which of our assumptions are most questionable.

Figure 3 compares the layer-averaged, KPP-based estimate of TKE production $\langle \Psi_{KPP} \rangle$ with the mean levels of observed dissipation $\langle \varepsilon_{obs} \rangle$. If $\langle \Psi_{KPP} \rangle$ should nearly balance or be less than the corresponding bulk dissipation, it is apparent that major discrepancies arise in the presence of strong vertical shear near the GS. For stations indicated in Figure 3 where $\langle Sh \rangle$ exceeds $4\langle \varepsilon_{obs} \rangle$, the layer-averaged observed dissipation tends to be an order of magnitude less than predicted using KPP.

In addition to random uncertainties stemming from limitations of the data set sampling, there may be three possible sources of systematic error in KPP-based production estimate for the high-shear mixed layer regime: (1) the boundary depth D may not be correctly

reproduced with the bulk Richardson number criteria, (2) KPP was designed to reproduce mixed layer fluxes in a horizontally homogeneous environment and needs to be modified here and (3) our assumption of steady-state TKE balance does not hold because of additional processes not considered. In the rest of the paper, we will explore these as possible reasons for the discrepancies.

3. Adjustment for boundary layer depth

a. Empirical boundary layer depths

If both the TKE balance assumption (4) and KPP are valid, it may be that applying Ri_{bulk} criteria (2) in station profiles does not predict the boundary layer depth in high shear environments, resulting in the TKE budget discrepancies. To examine this possibility, we compute two empirical boundary layer depths based on microscale dissipation measurements to compare with the KPP-diagnosed layer depth D_{Ri}. D_ε is defined as the depth where observed dissipation, smoothed over 4 m, drops to 2% of its boundary layer mean. The choice of 2% produces a clear demarcation of the mixing layer because it bisects the nearly three orders of magnitude between typical mixed layer and background dissipation rates here. It most accurately locates the sharp drop-off in $\log_{10}(\varepsilon)$ while minimizing interference from turbulent variability in the lower layer (e.g., Fig. 2a). In the case of free convection with $\langle \varepsilon \rangle \cong J_b^0/2$, selecting $\varepsilon = 0.02\langle \varepsilon \rangle$ gives $J_b = -0.01 J_b^0$ or less, depending on mixing efficiency, at D_ε (see Mironov *et al.,* 2000; and related PART1 discussion). This is a point well below an entrainment buoyancy flux peak of $J_b \cong -0.2 J_b^0$. This depth D_ε therefore corresponds to the bottom of the entrainment zone, and a criterion slightly higher or lower than 2% does not significantly impact results. This "mixing depth" D_ε is adjusted manually in some cases to remove the effect of upper layer statistical fluctuations in ε (PART1). In addition to D_ε, we infer the KPP mixed layer depth by comparing its local, subsurface parameterization to empirical diffusivity predictions $K_\rho^{obs} = \Gamma\varepsilon/N^2$ for stratified turbulence, based on observed ε, stratification N^2, and a mixing efficiency of $\Gamma = 0.2$ (Osborn, 1980). Because the subsurface component of KPP, based on the local gradient Richardson number, is applied immediately below D_{Ri}, that depth is compared to the level D_K where K_ρ^{obs} drops below the maximum value of the KPP prediction in the stable thermocline ($\leq 5 \times 10^{-3}$ m^2 s^{-1}), and both K_ρ^{obs} and K_ρ^{KPP} are decreasing with depth. This depth D_K generally corresponds well to the depth where observed stratification becomes stronger, just below the well-mixed layer, at the top of the entrainment zone and close to the maximum entrainment flux depth.

Overall, the KPP-diagnosed boundary layer depth D_{Ri} is comparable with D_ε (Fig. 4a) and D_K (Fig. 4b). The diagnosis of D_{Ri} from observed profiles depends through (2) on the linear extrapolation of velocity and buoyancy profiles from 8 m to the surface to determine mean values above $D_{Ri}/10$. This contributes to the random scatter in comparisons with D_ε and D_K for shallower layer depths $D_{Ri} < 100$ m. Systematic errors due to the linear extrapolation of profiles where near-surface logarithmic behavior is expected would tend
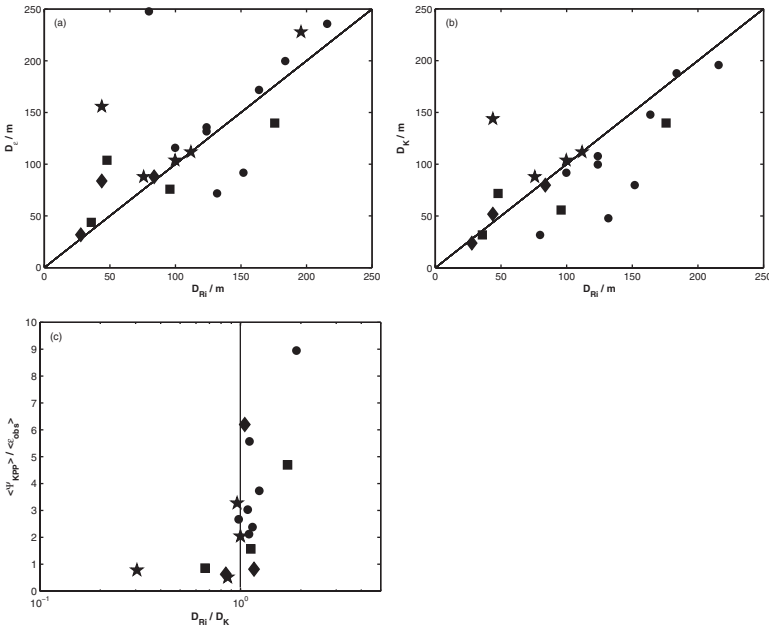
Figure 4. Predicted boundary layer depth from KPP D_{Ri} vs. observed boundary layer depth (a) D_ε and (b) D_K. (c) TKE budget ratio $\langle \Psi_{KPP} \rangle / \langle \varepsilon_{obs} \rangle$ vs. D_{Ri}/D_K. Solid lines indicate a ratio of 1. Symbols as in Figure 3.

to systematically underestimate D_{Ri}. This may explain a few cases in Figure 4b where D_{Ri} is less than D_K. However, attempting to correct for this extrapolation error would introduce greater random scatter. The biggest outlier is AMP21187 where $D_\varepsilon \sim 250$ m and $D_K \sim 30$ m (Fig. 4a and b), where the warmer water advected over the surface mixed layer (see Fig. 6 in PART1), and will not be used in further analysis below. The analysis of station AMP21199 (Fig. 5) is an example where $D_{Ri} < D_K = D_\varepsilon$. Here, energetic mixing persists further into the pycnocline than the mixed layer TKE production due to strong shear in the entrainment zone, and D_{Ri} may underpredict the layer depth indicated by the empirical diffusivity K_ρ^{obs}, which drops to the level of KPP's thermocline parameterization around D_ε.

At larger layer depths $D_{Ri} > 50$ m, there are two stations where D_{Ri} greatly overpredicts the inferred layer depth D_K, and no stations where $D_{Ri} \ll D_K$. Neither the random nor systematic errors from near-surface extrapolation offer compelling explanations of these large differences. In these cases D_{Ri} is also much greater than D_ε. Where D_{Ri} tends to be deeper than D_ε, there is strong shear through the boundary layer and this keeps the bulk Richardson number small going through the pycnocline. AMP21189 is an example of such a station (Fig. 6). Here, K_ρ^{obs} matches the KPP prediction above D_ε, D_K is around 50 m. Figure 4c plots the ratio $\langle \Psi_{KPP} \rangle / \langle \varepsilon_{obs} \rangle$ versus D_{Ri}/D_K, showing a relationship between the sign of the error in layer depth and the TKE budget discrepancy. This motivates the replacement of D_{Ri} by D_K in the KPP-based estimation of TKE production. Using D_K in
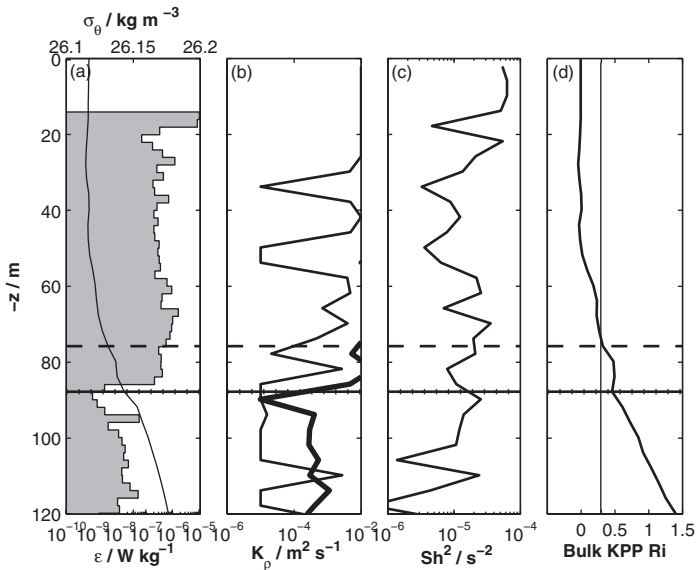
Figure 5. Vertical profiles in AMP21199. Horizontal dashed line is D_{Ri}, dotted line, D_K, overlies solid line D_ε. (a) Observed potential density averaged over 8 m and observed ε averaged over every 2 m, (b) vertical eddy diffusivity from KPP (thin) and K_ρ^{obs} (thick), (c) shear squared from 150 kHz ADCP, and (d) bulk Richardson number used in KPP. Vertical solid line indicates $Ri_b = 0.3$.

place of D_{Ri} in KPP removes what appears to be a systematic error in the estimation of layer depth, as well as reducing errors due to near-surface data extrapolations.

b. TKE budget adjusted for layer depth

With D_K substituted for D_{Ri} in the mixed layer formulations of K_ρ^{KPP}, K_ν^{KPP} and γ_b (Section 2a), fluxes and TKE production profiles were recomputed. Table 1 lists the bulk averages of shear and buoyant production estimates computed over the mixing depth interval $16\,\mathrm{m} \leq -z < D_\varepsilon$. Figure 7 compares the adjusted net production estimates to observed dissipation averaged over this entire resolved mixing layer (Fig. 7a) as well as separately over the mixed layer $16\,\mathrm{m} \leq -z < D_K$ (Fig. 7b) and the active pycnocline $D_K \leq -z < D_\varepsilon$ (Fig. 7c).

With the change in mixed layer definition to D_K, trends in $\langle J_b \rangle$ (Table 1) become more consistent with expectations, given $-L_{MO}$. When $-L_{MO}$ is larger than mixing layer depth D_K and D_ε (wind forcing is dominant and drives mixing), the buoyancy production $\langle J_b \rangle$ tends to be negative because of the work done in mixing local stratification. When $-L_{MO}$ is smaller, convection dominates and $\langle J_b \rangle$ is positive due to the contribution from surface buoyancy loss. If a shear-driven mixing layer penetrates deeply below D_K into a strong pycnocline above D_ε, TKE suppression by buoyancy flux due to the strong local stratification within the entrainment zone becomes more important. This improved corre-
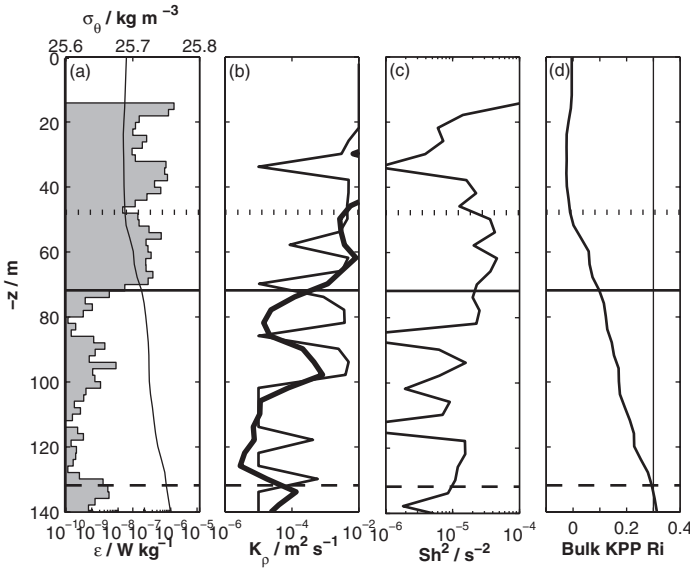
Figure 6. Same as Figure 5 but in AMP21189. Horizontal dashed line is D_{Ri}, dotted line, D_K, and solid line D_ε.

spondence arises due to the exclusion of high-shear transition zones below D_K from the depths wherein the larger nonlocal KPP parameterization of mixing is applied.

We note that ADCP measurements do not extend deep enough to allow us to define D_K in some high-shear boundary layer profiles, and these cases are excluded from our analysis, reducing the 21 stations of Figure 2 to the 19 listed in Table 1.

Although correcting the layer depth reduces the TKE budget discrepancy (Fig. 3) initially encountered, the same essential overestimate persists under strong shear with surface buoyancy loss: if $\langle J_b \rangle$ is positive and if the magnitude of $\langle Sh \rangle$ is large, the KPP estimate $\langle \Psi_{KPP} \rangle$ of TKE production tends to be up to one order larger than the bulk observed dissipation $\langle \varepsilon_{obs} \rangle$. This situation can occur under strong surface cooling in highly sheared mixed layers, where KPP appears to overestimate layer depth as D_{Ri} as well.

Bulk dissipation levels were compared to empirical predictions $\langle \varepsilon_{emp} \rangle$ of Lombardo and Gregg (1989) in Table 1. Over this data set, $\langle \varepsilon_{emp} \rangle / \langle \varepsilon_{obs} \rangle$ averaged 2.1. Although this empirical scaling was originally derived for $1 < -D/L_{MO} < 10$ (PART1), comparing mean $\langle \varepsilon_{obs} \rangle$ to the KPP production equivalent between 16 m $< -z < D_k$, $\langle \Psi_{KPP} \rangle / \langle \varepsilon_{obs} \rangle$, gives the similar value as 2.8 (Table 1).

4. Impacts of strong shear and baroclinicity on KPP diffusivities

This section examines several possible causes of the failure of the bulk TKE budget to close in sheared mixed layers. Assuming a vertically balanced budget (5), we consider two likely candidates not incorporated in KPP: the presence of strong shear due to baroclinicity

Table 1. Comparison between KPP and measurements within D_K. AMP drop number, the depth where diffusivity drops to thermocline value D_K, Monin-Obukhov length $-L_{MO}$, the surface buoyancy flux J_b^0, buoyancy production $\langle J_b \rangle = \dfrac{1}{D_K - 16} \int_{-D_K}^{-16} K_\rho^{KPP}(N^2 - \gamma_b)dz$, shear production from the purely wind-driven case $\langle Sh_{u*} \rangle = \dfrac{1}{D_K - 16} \int_{-D_K}^{-16} u_*^3/(\kappa z)dz$, shear production $\langle Sh \rangle = \dfrac{1}{D_K - 16} \int_{-D_K}^{-16} K_v^{KPP}|d\mathbf{V}/dz|^2 dz$, and averaged observed TKE dissipation rate, $\langle \varepsilon_{obs} \rangle = \dfrac{1}{D_K - 16} \int_{-D_K}^{-16} \varepsilon dz$, ratio $\langle \Psi_{KPP} \rangle/\langle \varepsilon_{obs} \rangle$ ($\langle \Psi_{KPP} \rangle = \langle J_b \rangle + \langle Sh \rangle$), empirical TKE dissipation rate Lombardo and Gregg (1989) $\overline{\varepsilon_{emp}} = 0.87(0.58 J_b^0 + 1.76\langle Sh_{u*} \rangle)$, ratio $\langle \varepsilon_{emp} \rangle/\langle \varepsilon_{obs} \rangle$, and symbols used in Figure 7. Bold type in ratios is used for stations where predictions exceed observations by a factor of 4.

AMP drop	D_k (m)	D_e (m)	$-L_{MO}$ (m)	J_b^0 (W kg^{-1})	$\langle J_b \rangle$ (W kg^{-1})	$\langle Sh_{u*} \rangle$ (W kg^{-1})	$\langle Sh \rangle$ (W kg^{-1})	$\langle \varepsilon_{obs} \rangle$ (W kg^{-1})	$\dfrac{\langle \Psi_{KPP} \rangle}{\langle \varepsilon_{obs} \rangle}$	$\langle \varepsilon_{emp} \rangle$ (W kg^{-1})	$\dfrac{\langle \varepsilon_{emp} \rangle}{\langle \varepsilon_{obs} \rangle}$	Symbol
21183	108	136	5	1.6e-7	1.3e-7	1.6e-8	1.8e-7	1.3e-7	2.30	1.0e-7	0.79	●
21184	92	116	32	4.8e-7	3.4e-7	3.6e-7	3.3e-7	2.5e-7	2.63	8.0e-7	3.14	●
21188	100	132	10	4.5e-7	2.3e-7	9.7e-8	1.5e-7	1.4e-7	2.83	3.8e-7	2.77	●
21189	48	72	24	5.8e-7	3.4e-7	4.8e-7	2.9e-7	3.2e-7	1.94	1.0e-6	3.20	●
21190	80	92	24	5.8e-7	4.3e-7	3.5e-7	9.4e-7	3.4e-7	**4.08**	8.3e-7	2.45	●
21191	56	76	17	6.1e-7	2.5e-7	3.2e-7	3.0e-7	2.2e-7	2.50	8.0e-7	3.58	■
21192	72	104	25	4.8e-7	1.6e-7	3.3e-7	4.7e-8	2.0e-7	1.02	7.5e-7	3.64	■
21193	32	44	41	3.0e-7	5.0e-8	5.4e-7	5.1e-7	6.6e-7	0.84	9.7e-7	1.47	■
21194	52	84	139	8.2e-8	4.5e-8	3.8e-7	4.1e-7	5.4e-7	0.85	6.2e-7	1.15	◆
21195	24	32	39	4.9e-8	−7.4e-8	9.7e-8	1.1e-6	1.7e-6	0.57	1.7e-7	0.10	◆
21196	20	56	50	5.7e-8	−2.7e-8	1.6e-7	5.3e-7	2.1e-7	2.43	2.8e-7	1.34	◆
21197	148	172	12	5.8e-7	7.2e-7	1.2e-7	2.9e-7	1.8e-7	**5.63**	4.7e-7	2.62	●
21198	112	112	37	4.5e-7	1.5e-7	3.4e-7	1.7e-6	9.3e-7	2.04	7.5e-7	0.81	★
21199	88	88	39	4.7e-7	8.7e-8	4.4e-7	5.3e-7	9.1e-7	0.68	9.0e-7	1.00	★
21204	104	104	43	4.8e-7	2.7e-7	4.4e-7	1.3e-6	4.5e-7	3.36	9.1e-7	2.01	★
21205	188	200	85	2.1e-7	2.0e-7	2.6e-7	5.3e-7	3.0e-7	2.45	5.1e-7	1.71	●
21207	80	88	200	2.1e-7	1.1e-7	1.0e-6	1.9e-6	4.0e-7	**5.11**	1.7e-6	**4.24**	◆
21208	140	140	59	3.7e-7	1.7e-7	3.8e-7	3.2e-6	2.9e-7	**11.62**	7.8e-7	2.65	■
21211	144	144	144	2.4e-7	−1.9e-8	6.0e-7	4.8e-7	6.5e-7	0.71	1.0e-6	1.59	●

or entrainment, and the effect of restratification due to cross-frontal advection on vertical diffusivity.

a. Nondimensional speed gradient profile

Although empirically adjusting the boundary layer definition used in KPP improves closure of the vertically integrated TKE budget, the diffusivities and TKE production still exceed observed dissipation. The vertical eddy diffusivity and viscosity in KPP are given by (3) and by functions of the velocity scale $w_\xi(\sigma) = \kappa u^*/\phi_\xi(\zeta)$, where ϕ_ξ is an empirical nondimensional gradient profile derived from atmospheric boundary layer observations
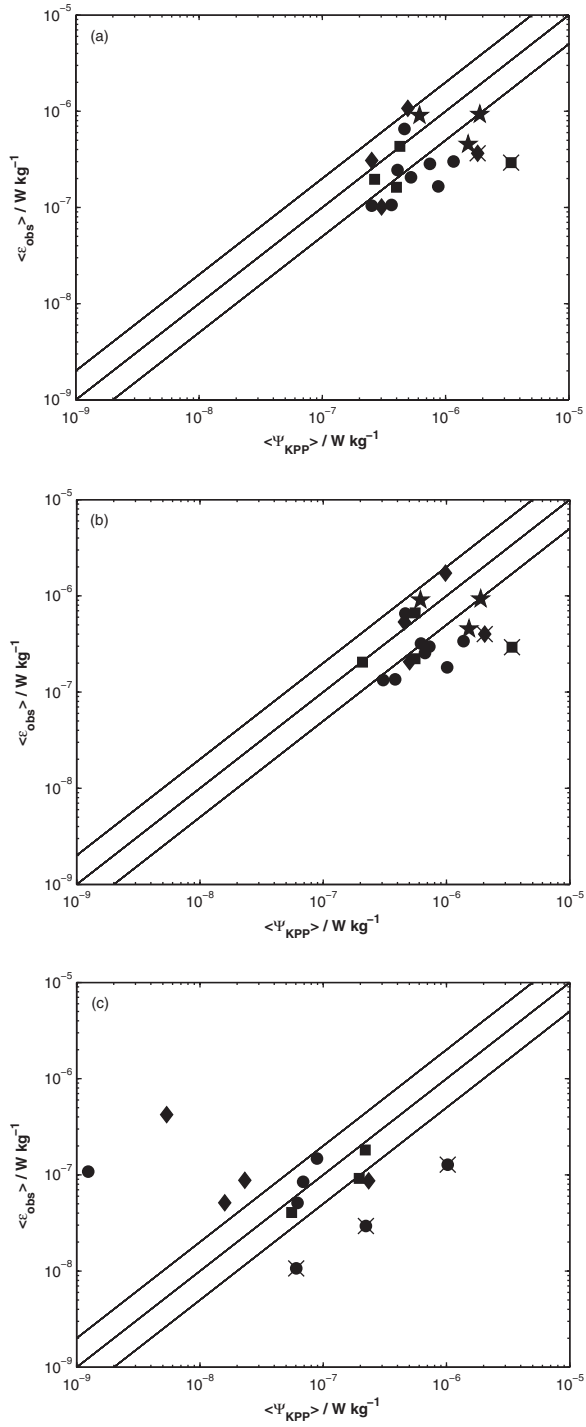
Figure 7

and $\zeta = -z/L_{MO}$. Here, $w_\xi(\sigma) = \kappa u*/\phi_\xi(0.1D/L_{MO})$ is used for the depth range of $0.1 < \sigma < 1$ so that the velocity scale of mixing within the boundary layer is set by surface forcing and D. While $w_\xi(\sigma)$ is constructed to reproduce these empirical scalings in the top part of the boundary layer under similar conditions (e.g., Vickers and Mahrt, 1999), the presence of substantial thermal wind shear, or shear due to submesoscale dynamics or entrainment would affect observed $\phi_\xi(\zeta)$, and the appropriate scaling of $w_\xi(\sigma)$ as well. Here, we compare the observed speed gradient profile

$$\phi_m(\zeta) = (-\kappa z/u*)\frac{\partial(U^2 + V^2)^{1/2}}{\partial z}, \tag{6}$$

to the empirical forms that constrain the choice of $w_\xi(\sigma)$ in KPP:

$$\begin{aligned}
\phi_m(\zeta) &= (1 - 16\zeta)^{-1/4}, && -0.2 \leq \zeta < 0, \\
\phi_m(\zeta) &= (1.26 - 8.38\zeta)^{-1/3}, && \zeta < -0.2.
\end{aligned} \tag{7}$$

Thus, nondimensional shear is scaled by the surface wind stress and buoyancy flux.

Figure 8 compares (7) with the observed speed gradient profile south of the GS for the station AMP21188. The observed speed gradient is much larger than (7) and does not follow (7) in the deeper layer. Figure 9 compares (6) and (7) averaged over boundary layer to depth D_K. Even with the diagnosed depth D_K, the magnitudes of observed speed gradient within the layer are larger than the empirical profiles.

Such departures are not unusual, but point to the underlying assumption of KPP that the velocity scales of large eddies dominating interior fluxes are set by the near-surface shear, and that interior shear production should therefore not differ significantly from predictions in cases conforming to (7). However, Figure 8 illustrates the pervasive mid-depth shears that elevate the mean levels at most stations in Figure 9, at weakly stratified depths where turbulence would be produced at large eddy length scales (i.e. $\sim D$). There are large speed gradients in the entrainment zone of AMP21188, but these are not expected to significantly export large eddies to set the interior $w_\xi(\sigma)$ scale, due to the shorter length and timescales of this production at stratified depths. They also do not contribute directly to layer-averaged production when using the corrected boundary layer depth.

Thermal wind shear, inertially resonant wind forcing and submesoscale turbulence could all contribute to elevated mid-depth shear. If, for example, strong mid-depth observed shear were due to baroclinicity, the impact of a geostrophic velocity scale $|\partial u^g/\partial z|D$ might be missing from the formulation of $w_\xi(\sigma)$. Another possibility is that transient or horizontally localized shear, observed or modeled at high temporal resolution, may not be well represented by KPP. Mean KPP momentum flux may be correct over

---

Figure 7. Bulk comparison between observed ϵ and predicted ϵ from KPP (a) within boundary layer, 16 m $< -z < D_\epsilon$, (b) within mixed layer, 16 m $< -z < D_K$, and (c) within transition zone, $D_K < -z < D_\epsilon$. Symbols, lines and crosses as in Figure 4.
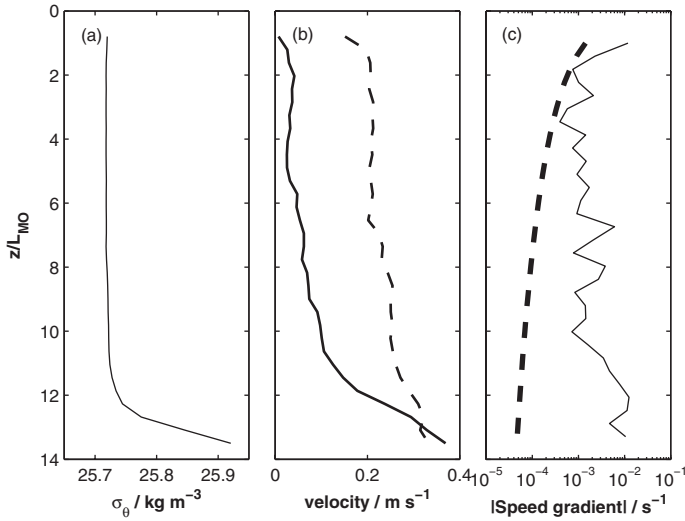
Figure 8. Vertical profiles in AMP21188 taken south of the Gulf Stream. Vertical axis is depth normalized by $-L_{MO} \sim 10$ m. (a) Observed potential density averaged over 8 m, (b) observed velocity profiles (u: solid and v: dashed) from 150 kHz ADCP, and (c) magnitude of dimensional vertical speed gradient, $u*/(-\kappa z) \times \phi_m(\zeta)$, from (7) (dashed) and that from observation (6).
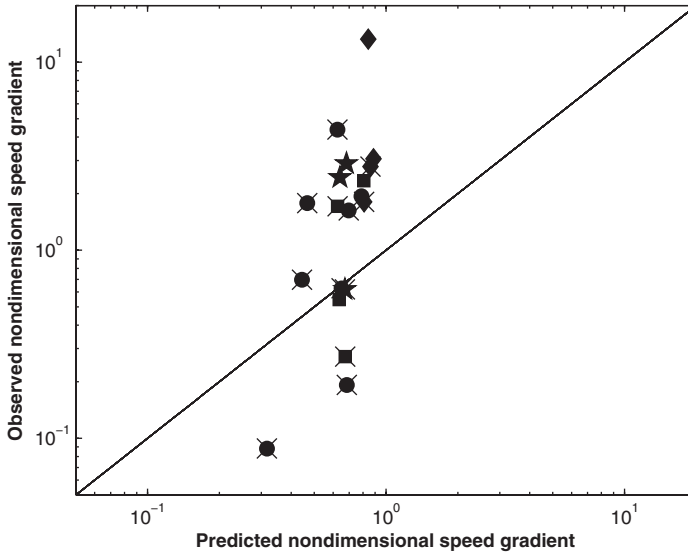

Figure 9. Comparison between observed non-dimensional speed gradient (6) and the empirical functions in KPP (7), averaged to depths D_K. Symbols are as in Figure 4 but negative averaged values of (6) are denoted by $+$.

larger or longer averages, while locally modeled TKE production at concentrated shears would suggest excessive net production, due to the absence of parameterized momentum flux transport divergence. Excessive TKE production estimates due to this possibility might therefore be resolved by successive inclusion of more nonlocal momentum gradients γ_u and γ_v (Smyth *et al.*, 2002; Noh *et al.*, 2003; Sorbjan, 2009) with increasing resolution, but only if this addition were accompanied by a successive reductions in K_v, allowing the nonlocal fluxes to vertically redistribute much of the surface stress.

b. *Effect of restratification*

In addition to the overprediction of production with KPP, observed ε is also similarly smaller than the empirical scaling reported by Lombardo and Gregg (1989) (PART1). Consistency with the KPP-derived ratios supports the view that some additional processes are suppressing turbulence near the GS front and reducing observed $\langle \varepsilon_{obs} \rangle$. Prime candidates for this suppression are restratification processes associated with lateral density gradients near fronts that could also add another sink to the TKE budget. If isopycnal slumping (Tandon and Garrett, 1995) occurs, or if mixed layer eddies (Fox-Kemper *et al.,* 2008) are formed during convection, these would cause re-stratification of the mixed layer concurrent with surface-driven mixing. Viscous stress acting on the thermal wind shears in the mixed layer (Thompson, 2000), and wind-driven Ekman transport (e.g., Thomas, 2005) could also cause re-stratification.

Thomas (2005) suggests that vertical fluxes within the boundary layer can be affected by those processes, and that the vertical velocity scale $w_\xi(\sigma)$ of KPP should account for them. Here, we simply modify the buoyancy velocity $w*^3 = J_b D_K$ to include the simultaneous effects of surface forcing and re-stratification under surface buoyancy loss,

$$w_{front}^{*3} = w*^3 + \int_{-D_K}^{0} \int_{-D_K}^{0} V^{ageo} \cdot \nabla_H b \, dz \, dz, \tag{8}$$

where V^{ageo} is the ageostrophic velocity driving re-stratification. With this generalization of the convective velocity we rewrite the Monin-Obukhov length scale,

$$L_{MO} = -\frac{u*^3}{\kappa J_b^0} = -\frac{D_K}{\kappa} \frac{u*^3}{w*^3} \Rightarrow L_{MO}^{front} = -\frac{D_K}{\kappa} \frac{u*^3}{w_{front}^{*3}}. \tag{9}$$

We use (7) here for $\phi_\xi(\zeta)$, but as discussed previously the form of (7) may also require changes. With (8), (3) is modified again to obtain a new K-profile incorporating restratification by V^{ageo}. Note that no additional sink terms are explicitly added to (5), because the use of observed shear and stratification in the KPP-based diagnoses already includes any ongoing effects below 16 m from V^{ageo} on these profiles in the shear and buoyant production terms.

Assuming a uniform lateral density gradient across the well-mixed layer, the maximum contribution to w_{front}^{*3} from surface wind-driven Ekman flow can be approximated as

$$\langle L^{Ekman} \rangle = \int_{-D_K}^{0} \int_{-D_K}^{0} V_{Ekman}^{ageo} \cdot \nabla_H b \, dz \, dz \approx \int_{-D_K}^{0} \frac{\tau_0 \cdot f d\mathbf{U}/dz}{\rho_0 f} \, dz, \tag{10}$$

by assuming the Ekman depth is much less than D_K. Here, $\nabla_H b = \partial b/\partial x + \partial b/\partial y$ and f is the Coriolis parameter. For re-stratification due to submesoscale eddies, lateral fluxes are parameterized by Fox-Kemper *et al.* (2008) in terms of an effective velocity V_{Eddy}^{ageo}, with constant C_e and a shape function described therein. Neglecting the shape function, the maximum contribution to w_{front}^{*3} would be

$$\langle L^{Eddy} \rangle = \int_{-D_K}^{0} \int_{-D_K}^{0} V_{Eddy}^{ageo} \cdot \nabla_H b \, dz \, dz \approx -\int_{-D_K}^{0} \frac{C_e \|\nabla_H b\|^2 D_K^2}{|f|} \, dz. \tag{11}$$

This parameterization represents re-stratification after a strong forcing event, and ageostrophic velocities concurrent with the strong surface forcing here may be different. Without modification, we take (11) as indicative of the maximum effect of ongoing re-stratification under these more persistent surface forcing conditions.

Stations AMP21190, 21192, and 21194 illustrate the effect of these modifications. These three profiles are representative of $\langle \Psi_{KPP} \rangle > \langle \varepsilon_{obs} \rangle$ cases south of the GS (AMP21190), $\langle \Psi_{KPP} \rangle \cong \langle \varepsilon_{obs} \rangle$ cases in the GS (AMP21192), and $\langle \Psi_{KPP} \rangle < \langle \varepsilon_{obs} \rangle$ cases north of the GS (AMP21194). The lateral density gradient in the boundary layer is estimated by the centered finite differentiation of the sea-surface densities from CTD data simultaneous with microstructure measurements. Due to the limitation of measurements taken along a single cross-frontal transect, we assume that the density gradients are oriented closely along the section line (S1 in Fig. 1). Results using the above parameterizations to adjust w^{*3} in these three example cases for the surface wind-driven Ekman flow are listed in Table 2b, and for submesoscale eddies in Table 2c. Re-stratification due to the viscous stress acting on the thermal wind shear (Hallberg, 2003) and that due to the slumping isopycnal surface (Tandon and Garrett, 1995) share the same similarity scaling with $\|\nabla_H b\|^2/f$ as in (11).

Figure 10 shows the modified $w_m(\sigma)$ and $K_m(\sigma)$ profiles obtained by applying the changes from (10)–(11) to the dependence on w^{*3} in (3). In several cases, the predictions are slightly better (Table 2a). The largest re-stratification effect is estimated for AMP21194 by Ekman advection where L_{MO} and L_{MO}^{front} have different signs. However, the magnitude of improvement in K_ξ through (7) is even less than $(w_{front}^{*3})^{1/3}$, making this change much too small to account on its own for the TKE budget discrepancy in Figures 7 and 10, and Table 1. Although there are large uncertainties in these modification methods of KPP (e.g., using (7) for positive L_{MO}^{front} in AMP21194), the comparisons do not support the possibility that large TKE budget discrepancies can be accounted for here by including baroclinic restratification effects in the KPP w^* scale.

Table 2. Results of KPP diagnosis incorporating restratification due to Ekman advection and submesoscale processes.

A. Original KPP

AMP drop	$-L_{MO}$ (m)	w^{*3} (m³ s⁻³)	$\langle J_b \rangle$ (W kg⁻¹)	$\langle Sh \rangle$ (W kg⁻¹)	$\langle \varepsilon_{obs} \rangle$ (W kg⁻¹)	$\dfrac{\langle \Psi_{KPP} \rangle}{\langle \varepsilon_{obs} \rangle}$	Wind (dir °)
21190	24	4.6e-5	4.3e-7	9.4e-7	3.4e-7	4.08	123.5
21192	25	3.5e-5	1.6e-7	4.7e-8	2.0e-7	1.02	111.9
21194	139	4.2e-6	4.5e-8	4.1e-7	5.4e-7	0.85	98.8

B. Ekman advection

AMP drop	$-L_{MO}^{front}$ (m)	$\langle L^{Ekman} \rangle$ (m³ s⁻³)	$\langle J_b \rangle$ (W kg⁻¹)	$\langle Sh \rangle /$ (W kg⁻¹)	$\dfrac{\langle \Psi_{KPP} \rangle}{\langle \varepsilon_{obs} \rangle}$ (m)
21190	25	−2.9e-6	4.3e-7	9.3e-7	4.02
21192	10	5.3e-5	9.8e-8	5.7e-8	0.76
21194	−50	−1.6e-5	7.6e-8	1.3e-7	0.40

C. Submesoscale eddy

AMP drop	$-L_{MO}^{front}$ (m)	$\langle L^{Eddy} \rangle$ (m³ s⁻³)	$\langle J_b \rangle$ (W kg⁻¹)	$\langle Sh \rangle$ (W kg⁻¹)	$\dfrac{\langle \Psi_{KPP} \rangle}{\langle \varepsilon_{obs} \rangle}$
21190	24	−1.4e-6	4.3e-7	9.4e-7	4.05
21192	48	−1.7e-5	1.9e-7	4.2e-8	1.13
21194	201	−1.3e-6	4.7e-8	4.0e-7	0.84

5. Impacts of internal waves and submesoscale processes on the bulk TKE budget

If the modifications of KPP in Section 4 are of no avail, another possible source of TKE budget discrepancies is that the bulk TKE balance (5) is not valid in the mean. Here we examine possible contributions to a mean local imbalance from internal wave radiation and submesoscale dynamics on (5).

Loss of energy by near-inertial internal wave radiation may have a significant impact. In less baroclinic environments, the concentration of near-inertial internal wave energy would be expected to come out of the budget of near-inertial mixed layer bulk energy $|\langle \mathbf{U} \rangle|/2$, rather than the energy $|\mathbf{U} - \langle \mathbf{U} \rangle|^2/2$ of the shear profile that contributes to $\langle \Psi_{KPP} \rangle$ through higher frequency turbulent motions. Mixed layer eddy formation mechanisms, such as symmetric instabilities, involve near-inertial motions that displace the layer bottom and could thereby rapidly radiate energy downward in short wavelength, near-inertial internal waves. The downward flux $\bar{\Phi}_z|_{-D}$ of this energy by pressure-velocity correlations at near-inertial frequencies would be consistent with the observed properties of elevated internal wave energy reported in PART1. High dissipation rates in the permanent thermocline averaged $O(10^{-8}) \sim O(10^{-7})$ W kg⁻¹, at least an order of magnitude
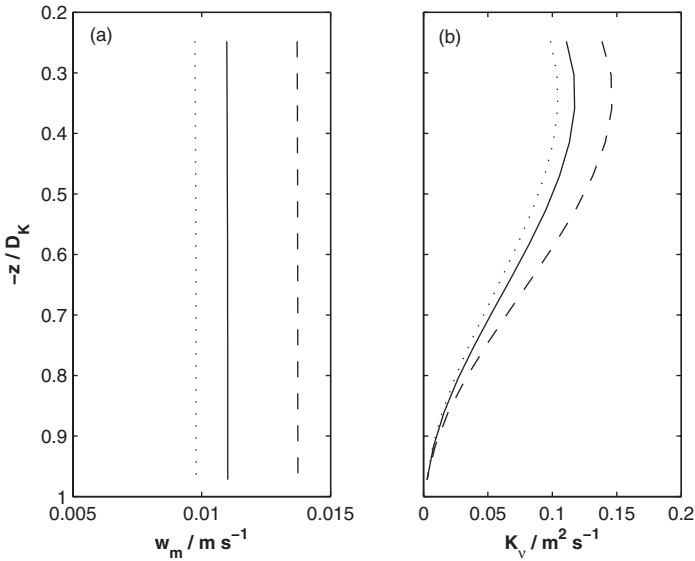
Figure 10. Vertical profiles in AMP21192 taken inside the Gulf Stream. (a) Velocity scale for momentum w_m, and (b) KPP vertical eddy viscosity K_ν within the boundary layer. Solid lines are without any re- or de-stratification effect. Dotted lines are the modified profiles by eddy re-stratification (Fox-Kemper *et al.,* 2008). Dashed lines are that by Ekman driven flow (Thomas, 2005).

smaller than the $O(10^{-6})$ W kg^{-1} TKE budget discrepancy, in the mixed layer. Integrated over a few-hundreds-meter-thick thermocline, elevated levels of deep pycnocline dissipation, reported in PART1 to be consistent with the observed internal waves shear spectrum, would constitute roughly 10% of the largest mixed layer TKE budget discrepancies. Allowing for local redistribution and some fraction of radiation away from the front could conceivably account for a substantial fraction of the dissipation apparently missing from the mixed layer.

Another possible source for the TKE budget discrepancy lies in the dynamics of the submesoscale eddies. These O(1–10) km structures may form in baroclinic environments by several different mixed layer instability mechanisms (Bocaletti *et al.,* 2007). After formation they may grow in horizontal scale and thereby entail an inverse cascade of energy to larger scales, rather than the forward cascade to the observed microscales. In addition, these eddies move away from the front after formation and therefore there is a horizontal divergence of kinetic energy, violating the vertical balance assumptions of our TKE budget analysis. The growth of energy in submesoscale eddies is driven by the release of gravitational potential energy from the baroclinic density field by instabilities that carry and are driven by lateral buoyancy fluxes across the front. Although the indirect contribution of this process through $w_\xi(\sigma)$ in KPP was small (i.e., $\sim w^*_{front}$ in Section 4b), the direct effect on the TKE budget would be much larger (i.e., $\sim w^{*3}_{front}$).

We are unable to broadly specify lateral density gradients directly from observed hydrography across this data set. Even if the hydrographic sections were at known angles

to lateral mixed layer density gradients, stations at 20-km intervals provide limited information about local buoyancy gradients at the $O(1–10)$ km submesoscales typical of sharp surface fronts. We therefore turn to an available proxy that assumes the predominant persistence of central mixed layer thermal wind shear under observed surface forcing conditions. We use this estimate

$$\partial \mathbf{u}^{\sim g}/\partial z \equiv \frac{2}{D_K} \int_{-3D_K/4}^{-D_K/4} \partial \mathbf{U}/\partial z \, dz \tag{12}$$

as a proxy for a mean thermal wind shear $\partial \mathbf{u}^g/\partial z$ with $|\partial \mathbf{u}^g/\partial z| = \|\nabla_H b\|/|f|$, to examine the possibility that TKE budget discrepancies depend on baroclinic submesoscale dynamics. We assume that in the central half of the mixed layer shear driven by surface forcing is small. Due to near-surface ADCP depth limits we use only profiles with $D_K > 28$ m. Comparing concurrent nearby 75-kHz ADCP measurements and horizontal density gradients from 100–300 m, Joyce *et al.* (2009) report that the deeper velocities were close to geostrophic balance. However, the correspondence suggested here for the upper ocean is loose, as $|\partial u^{\sim g}/\partial z|$ may be significantly reduced from the geostrophically balanced shear $\|\nabla_H b\|/|f|$ by vertical mixing above D_K. As expected for the CLIMODE cruise, if there is strong near-inertial shear within the lower mixed layer, $|\partial u^{\sim g}/\partial z|$ can be larger than $\|\nabla_H b\|/|f|$. Figure 9 indicates $|\partial u^{\sim g}/\partial z|$ is typically much larger than the $O(u*/D_K)$ scale expected for wind-driven shear turbulence. If we adopt this tenuous assumption, then for layers well mixed in density but not shear, the potential vorticity $PV \cong \langle fN^2 + \partial U/\partial z \cdot \partial b/\partial y - \partial V/\partial z \cdot \partial b/\partial x \rangle$ is approximately $-f|\partial \mathbf{u}^{\sim g}/\partial z|^2$.

Figure 11 rescales the both the KPP and empirical discrepancies $\Delta \varepsilon_{KPP} = \langle \Psi_{KPP} \rangle - \langle \varepsilon_{obs} \rangle$ and $\Delta \varepsilon_{emp} = \langle \varepsilon_{emp} \rangle - \langle \varepsilon_{obs} \rangle$, plotting $(\Delta \varepsilon/D_K^2)$ versus $f|\partial \mathbf{u}^{\sim g}/\partial z|^2 \cong -PV$. Negative values of $\Delta \varepsilon$, possibly due to either unresolved near-surface production processes or statistical scatter, are neglected here. While the scatter among the positive data from both comparisons is large, they do seem to suggest that, relative to expectations, observed dissipation levels are decreasing with shear and with negative potential vorticity. The rate of baroclinic energy release associated by Fox-Kemper *et al.* (2008) with the buoyancy flux carried by these eddies ((11), rescaled by D_K) is plotted in Figure 11, substituting $|\partial \mathbf{u}^{\sim g}/\partial z|^2$ for $\|\nabla_H b\|^2/f^2$. The slope of this parameterization, 1, is steeper than indicated by either set of positive $\Delta \varepsilon$ points. However, if $|\partial \mathbf{u}^{\sim g}/\partial z|^2$ underestimates $\|\nabla_H b\|^2/f^2$ somewhat due to some turbulent mixing of thermal wind shear, the comparison suggests these submesoscale dynamics and associated internal wave processes could be related to the reduced mixed layer dissipation rates. If observed shear $\partial \mathbf{U}/\partial z$ is due to submesoscale turbulence, overall consistency between $\Delta \varepsilon_{KPP}$ and $\Delta \varepsilon_{emp}$ may support the suggestion that TKE is lost from the mixed layer budget by the radiative transport or inverse cascade process.

It is also possible that wind-driven Ekman flow generates submesoscale eddies (Thomas, 2008) and could add additional terms in the TKE budget. To explore this possibility, Figure 12a shows the dependence of the ratio, $\langle \Psi_{KPP} \rangle/\langle \varepsilon_{obs} \rangle$, on differences between wind and surface
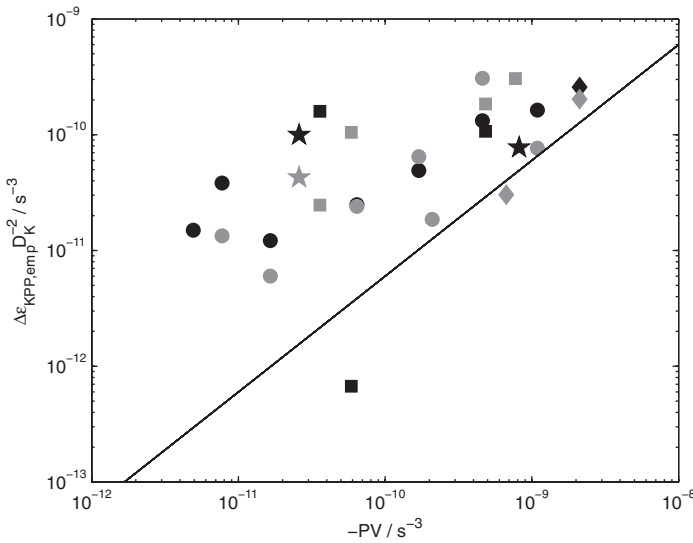
Figure 11. Dependence of normalized dissipation rate differences on $f|\partial \mathbf{u}^{\sim g}/\partial z|^2 \cong -PV$. Symbols as in Figure 7, with $\Delta\varepsilon_{KPP} = \langle \Psi_{KPP} \rangle - \langle \varepsilon_{obs} \rangle$ in black and $\Delta\varepsilon_{emp} = \langle \varepsilon_{emp} \rangle - \langle \varepsilon_{obs} \rangle$ in gray. Only $\Delta\varepsilon_{KPP} > 0$ and $\Delta\varepsilon_{emp}$ are shown. The solid line indicates the potential energy release associated with the Fox-Kemper *et al.* (2008) rate of restratification by submesoscale eddies (11) as a function of $f|\partial \mathbf{u}^g/\partial z|^2$.

front directions, diagnosed again on the assumption that $\partial \mathbf{u}^{\sim g}/\partial z$ points downfront. Although the number of samples is limited and we see large scatter, there is a tendency that the ratios are closer to 1 when Ekman flow brings dense water over lighter water and that the largest deficits in $\langle \varepsilon_{obs} \rangle$ occur when the wind would be blowing towards the inferred downgradient direction of surface density, 90 degrees left of the mixed layer shear. Figure 12b plots the deficit $\Delta\varepsilon$ from empirical and KPP-based expectation against the maximum estimated contribution $J_b^{Ek} = -(\bar{\tau}_0 \cdot \partial \mathbf{u}^{\sim g}/\partial z)/\rho_0$ to buoyant TKE production from Ekman advection, showing no clear correlation. Figure 12c shows that there is instead more of a correlation with an O(1) slope between $\Delta\varepsilon$ and a conjugate quantity $J_b^{nonEk} = \hat{k} \cdot (\bar{\tau}_0 \times \partial \mathbf{u}^{\sim g}/\partial z)/\rho_0$, that is a maximum for winds blowing down the inferred surface density gradient.

We have considered the implications of assuming that $\partial \mathbf{u}^{\sim g}/\partial z$ is related to baroclinicity through geostrophic balance, but this is not the only possible interpretation. If instead it is due to entrainment driven by mixed layer inertial oscillations, then either Figure 11 or Figures 12a and c suggest this process is not well-modeled by KPP. A more complete time series of this process may show the sampling of the angle between wind and inertially oscillating shear in Figure 12 is statistically skewed, and that uniformly averaging over the angle will reduce the average discrepancy. Even so, the phase dependence for the TKE discrepancy suggested in Figure 12c could significantly impact the submesoscale and subinertial timescale dynamics using KPP.
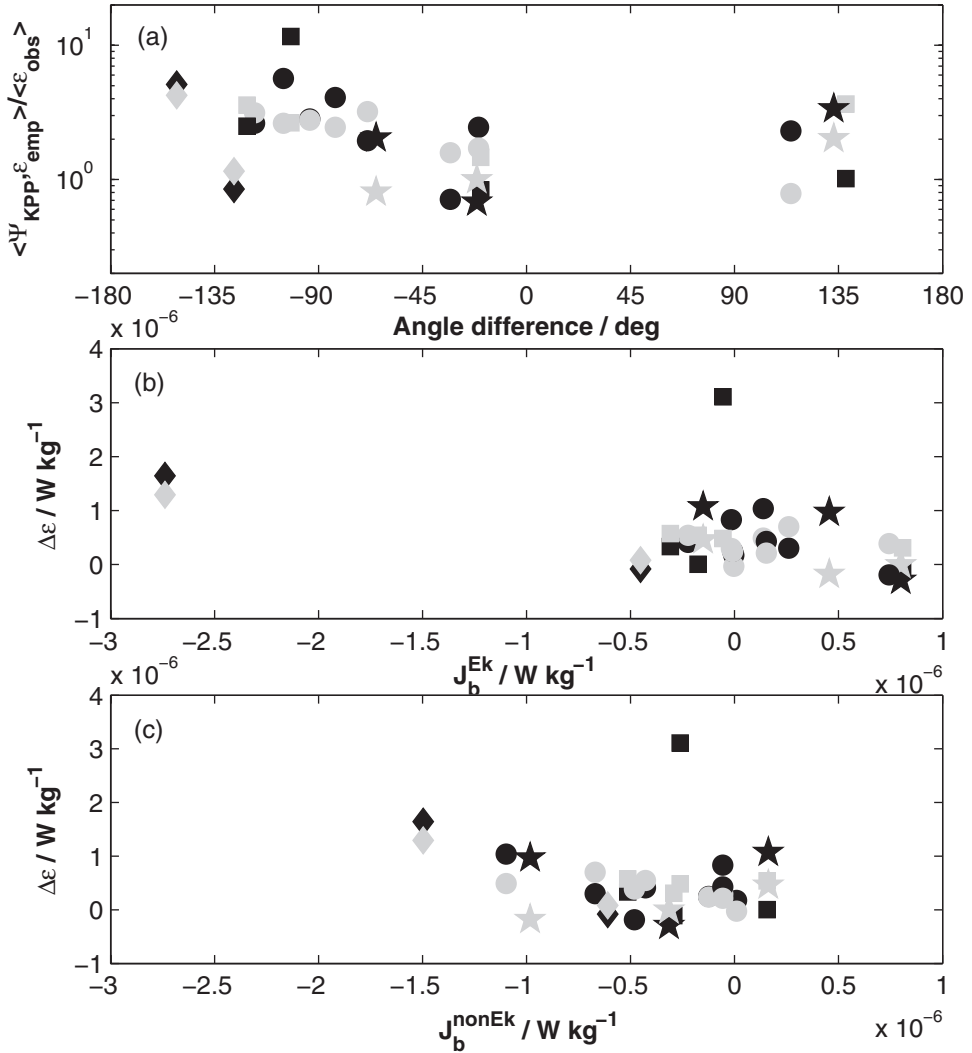
Figure 12. (a) The ratio of observed dissipation rate to predicted values against differences between current and wind directions, (b) differences between observed and predicted dissipations against buoyancy flux due to Ekman transport, and (c) differences between observed and predicted dissipations against buoyancy flux due to wind transport without earth rotation. Black is the KPP prediction. Gray is the empirical scaling. Symbols as in Figure 3.

6. Summary and conclusion

We have evaluated the mixed layer TKE budget production terms using the K-profile parameterization (Large *et al.,* 1994) and in-situ CTD, ADCP, and microstructure measurements taken during a CLIMODE winter cruise in February 2007. Our analysis sets a lower

bound for the discrepancy between KPP-based predictions of TKE production and the observed dissipation rates assuming that a near-equilibrium balance of production and dissipation holds when the TKE budget is averaged over the boundary layer. Boundary layer depth prediction, TKE budget at the entrainment zone, and non-dimensional speed gradient profile are also compared with observation. Effects of baroclinic lateral density gradients on K-profiles and on the TKE budget are investigated. Detailed results may be summarized as follows:

- Strong shear within the boundary layer can result in an excessively deep diagnosis of boundary layer depth D_{Ri} under the KPP bulk Richardson number criteria. This results in erroneously high mixing and TKE production rates when the boundary layer K-profile is applied within the highly sheared entrainment zone of mixed layer. The examination by Noh *et al.* (2003) of the diagnosis of D_{Ri} in the atmospheric precursor (Troen and Mahrt, 1986) of KPP arrived at similar conclusions on the effect of shear on D_{Ri}.

- Although modification of boundary layer depth can exclude the entrainment zone and reduce the estimated TKE production, a substantial budget discrepancy remains. The discrepancy may be due to the $O(1)$ hour time scale of station profile mean shears, which corresponds to spatial-temporal scales in high resolution process models that invoke KPP. This might be resolved by the combined inclusion of a nonlocal momentum flux gradient and a reduction in eddy viscosity with increasing resolution.

- Observed dissipation is also smaller than the empirical scaling of ε within the mixed layer according to Lombardo and Gregg (1989), a diagnosis independent of KPP or measurement timescales. This coincidence with the elevated diagnosis from KPP suggests that either the actual TKE production is reduced, or that additional TKE loss processes undermine budget closure assumptions.

- The possibility of turbulence suppression by ongoing baroclinic restratification processes was examined, incorporating lateral density gradients into the convective velocity scale of KPP, $w*$. However, the estimated effect on $w*$ did not significantly resolve the TKE budget discrepancy.

- Another possibility, noted but not fully resolved here, is that a substantial fraction of shear energy in observed mixed layers is associated with submesoscale instabilities and eddies that do not dissipate locally, but cascade instead to larger horizontal scales while transporting energy away from fronts, or radiating energy downward though internal waves to enhance dissipation in the pycnocline. Those processes could significantly undermine local TKE budget balance assumptions. Comparisons between the diagnosed TKE budget discrepancy and the energy released through submesoscale lateral buoyancy fluxes in the parameterization of Fox-Kemper *et al.* (2008) and between wind-driven Ekman flux (Thomas, 2005) and current/wind directions are not statistically conclusive, but they do suggest some possible explanations for low levels of observed microscale dissipation. These comparisons are perhaps more important for what they do not show here, such as enhanced mixed layer

turbulence levels near fronts or in downfront wind conditions. Assessing impacts of lateral density gradients on mixed layer turbulence would be improved if the spatial and temporal resolutions of measurements were sufficient to evaluate thermal wind shear and separate inertial motion in observed mixed layers. A significantly larger number of samples might also permit greater accuracy in the determination of means from observables with nearly lognormal distributions.

REFERENCES

Alford, M. H. 2001. Internal swell generation: The spatial distribution of energy flux from the wind to mixed-layer near-inertial motions. J. Phys. Oceanogr., *31,* 2359–2368.

Boccaletti, G., R. Ferrari and B. Fox-Kemper. 2007. Mixed layer instabilities and restratification. J. Phys. Oceanogr., *37,* 2228–2250.

Burchard, H. and K. Bolding. 2001. Comparative analysis of four second-moment turbulence closure models for the oceanic mixed layer. J. Phys. Oceanogr., *31,* 1943–1968.

Capet, X., J. C. McWilliams, M. J. Molemaker and A. F. Shchepetkin. 2008. Mesoscale to submesoscale transition in the California Current System. Part I: Flow structure, eddy flux, and observational tests. J. Phys. Oceanogr., *38,* 29–43.

CLIMODE Group: J. Marshall, A. Andersson, N. Bates, W. Dewar, S. Doney, J. Edson, R. Ferrari, G. Forget, D. Fratantoni, M. Gregg, T. Joyce, K. Kelly, S. Lozier, R. Lumpkin, G. Maze, J. Palter, R. Samelson, K. Silverthorne, E. Skyllingstad, F. Straneo, L. Talley, L. Thomas, J. Toole and R. Weller, 2009. The Climode Field Campaign: Observing the Cycle of Convection and Restratification over the Gulf Stream. Bull. Amer. Meteor. Soc., *90,* 1337–1350.

D'Asaro, E. A., C. C. Eriksen, M. A. Levine, P. Niiler, C. A. Paulson and P. van Meurs. 1995. Upper ocean inertial currents forced by a strong storm. Part I: Data and comparisons with linear theory. J. Phys. Oceanogr., *25,* 2909–2936.

Fox-Kemper, B., R. Ferrari and R. W. Hallberg. 2008. Parameterization of mixed layer eddies. Part I: Theory and diagnosis. J. Phys. Oceanogr., *38,* 1145–1165.

Gregg, M. C. 1999. Uncertainties and limitations in measuring ε and χ_T. J. Atmos. Oceanic. Technol., *16,* 1483–1490.

Hallberg, R. 2003. The suitability of large-scale ocean models for adapting parameterizations of boundary mixing and a description of a refined bulk mixed layer model, *in* Proceedings of the 2003 'Aha Huliko'a Hawaiian winter workshop, P. Muller and D. Henderson, eds., U. Hawaii, 187–203.

Inoue, R., M. C. Gregg and R. R. Harcourt. 2010. Mixing rates across the Gulf Stream, Part 1: On the formation of Eighteen Degree Water. J. Mar. Res., *68,* 643–671.

Joyce, T. M., L. N. Thomas and F. Bahr. 2009. Wintertime observations of Subtropical Mode Water formation within the Gulf Stream. Geophys. Res. Lett., *36,* L02607, doi:10.1029/2008GL035918.

Kantha, L. H. and C. A. Clayson. 2003. On the effect of surface gravity waves on mixing in an oceanic mixed layer model. Ocean Model., *6,* 101–124.

Large, W. G. and P. R. Gent. 1999. Validation of vertical mixing in an equatorial ocean model using large eddy simulations and observations. J. Phys. Oceanogr., *29,* 449–464.

Large, W. G., J. C. McWilliams and S. C. Doney. 1994. Oceanic vertical mixing: A review and a model with a nonlocal boundary layer parameterization. Rev. Geophys., *32,* 363–403.

Lombardo, C. P. and M. C. Gregg. 1989. Similarity scaling of viscous and thermal dissipation in a convecting surface boundary layer, J. Geophys. Res., *94,* 6273–6284.

Marshall, J. 2005. CLIMODE: A mode water dynamics experiment in support of CLIVAR. U.S. Clivar Variations, *3,* 8–14.

McWilliams, J. C., P. P. Sullivan and C. H. Moeng. 1997. Langmuir turbulence in the ocean. J. Fluid Mech., *334,* 1–30.

Mellor, G. L. and T. Yamada. 1982. Development of a turbulence closure model for geophysical fluid problems. Rev. Geophys., *20,* 851–875.

Mironov, D. V., V. M. Gryanik, C.-H. Moeng, D. J. Olbers and T. H. Warncke. 2000. Vertical turbulence structure and second-moment budgets in convection with rotation: A large-eddy simulation study. Q. J. R. Meteorol. Soc., *126,* 477–515.

Niiler, P. P. and E. B. Kraus. 1977. One-dimensional models, *in* Modeling and Prediction of the Upper Layers of the Ocean, E. B. Kraus, ed., Pergamon, NY, 143–172.

Noh, Y., W. G. Cheon, S.-Y. Hong and S. Raasch. 2003. Improvement of the K-profile model for the planetary boundary layer based on large eddy simulation data. Bound.-Layer Meteor., *107,* 401–427.

O'Brien, J. J. 1970. A note on the vertical structure of the eddy exchange coefficient in the planetary boundary layer. J. Atmos. Sci., *27,* 1213–1215.

Osborn, T. R. 1980. Estimates of the local rate of vertical diffusion from dissipation measurements. J. Phys. Oceanogr., *10,* 83–89.

Peters, H. and H. Z. Baumert. 2007. Validating a turbulence closure against estuarine microstructure measurements. Ocean Model., *19,* 183–203.

Polton, J. A., J. A. Smith, J. A. MacKinnon and A. E. Tejada-Martinez. 2008. Rapid generation of high-frequency internal waves beneath a wind and wave forced oceanic surface mixed-layer. Geophys. Res. Lett., *35,* doi:10.1029/2008GL033856.

Shay, T. and M. C. Gregg. 1986. Convectively driven turbulent mixing in the upper ocean. J. Phys. Oceanogr., *16,* 1777–1798.

Smyth, W. D., E. D. Skyllingstad, G. B. Crawford and W. Hemantha. 2002. Nonlocal fluxes and Stokes drift effects in the K-profile parameterization. Ocean Dyn., *52,* 104–115.

Sorbjan, Z. 2009. Improving non-local parameterization of the convective boundary layer. Bound.-Layer Meteor., *130,* 57–69.

Tandon, A. and C. Garrett. 1995. Geostrophic adjustment and restratification of a mixed layer with horizontal gradients above a stratified layer. J. Phys. Oceanogr., *25,* 2229–2241.

Thomas, L. N. 2005. Destruction of potential vorticity by winds. J. Phys. Oceanogr., *35,* 2457–2466.

—— 2008. Formation of intrathermocline eddies at ocean fronts by wind-driven destruction of potential vorticity. Dyn. Atmos. Oceans., *45,* 252–273.

Thompson, L. 2000. Ekman layers and two-dimensional frontogenesis in the upper ocean. J. Geophys. Res., *105,* 6437–6451.

Troen, I. and L. Mahrt. 1986. A simple model of the atmospheric boundary layer; sensitivity to surface evaporation. Bound.-Layer Meteor., *37,* 129–148.

Vickers, D. and L. Mahrt. 1999. Observations of non-dimensional wind shear in the coastal zone. Quart. J. Roy. Meteor. Soc., *125,* 2685–2702.

Worthington, L. V. 1959. The 18° water in the Sargasso Sea. Deep-Sea Res., *5,* 297–305.